The Limit of Spin Lifetime in Solid-State Electronic Spins.

Supporting Information.

Alessandro Lunghi* and Stefano Sanvito

School of Physics, AMBER and CRANN Institute, Trinity College, Dublin 2, Ireland

E-mail: lunghia@tcd.ie

Computational Methods

Lattice Dynamics

All the structural optimisation and force constants calculations were previously presented.[1] Being $\Phi_{ij}(lm)$ the force constant, coupling the i-th atomic degrees of freedom in the lattice cell at the position R_l and the j-the atomic degrees of freedom in the lattice cell of position R_m, the dynamical matrix, $\mathbf{K}(\mathbf{q})$, at the $\mathbf{q}$-point, is built as

$$K_{ij}(\mathbf{q}) = \sum_l \Phi_{ij}(l0) e^{i\mathbf{q}\cdot\mathbf{R}_l} \,, \tag{1}$$

where the sum runs over all the infinite periodic cells of the crystal. The eigenvalues of $\mathbf{K}(\mathbf{q})$ are $\omega^2(\mathbf{q})$, while the eigenvectors $\mathbf{L}(\mathbf{q})$ defines the normal modes of vibration.

Magnetic Properties Calculations

The ORCA software[2] has been employed for the calculation of the $\mathbf{g_e}$ and $\mathbf{A}$ tensors for both equilibrium and distorted geometries. We have used the basis sets def2-TZVP for V and O, def2-SVP for C and H and a def2-TZVP/C auxiliary basis set for all the elements. For the calculation of the $\mathbf{A}$ tensors the entire basis set have been de-contracted. The calculations of the $\mathbf{g_e}$ tensors have been carried out at both the DFT level, with the PBE functional,[3] and at the CASSCF+NEVPT2 level of theory, with a (1,5) active space and spin-orbit contributions included through quasi-degenerate perturbation theory. The calculations of the $\mathbf{A}$ tensors have been performed at the DFT level with the PBE functional.

Machine Learning Training and Test Sets Generations

The training sets for the machine learning (ML) models have been generated by calculating both $\mathbf{g_e}$ and $\mathbf{A}$ for 2600 distorted structures. The distorted structures were obtained by displacing all the Cartesian coordinates of all the atoms of the DFT optimized geometry

of $VO(acac)_2$ by a random value within the interval [-0.05Å: 0.05Å] for 1300 structures and [-0.01Å: 0.01Å] for the remaining 1300 structures. Among the total of 2600 distorted geometries, 1800 were used for training the ML models, while 800 were used for testing.

Supervised Machine Learning.

Following a recent proposal for the ML modelling of magnetic properties,[4] both the tensors $\mathbf{g_e}$ and $\mathbf{A}$ have been decomposed into spherical tensors of order 0 (T^0) and 2 (T^m), where the index m runs over the five component of the tensor. The spherical tensors are decomposed into atomic contributions and then written as function of atomic environment fingerprints, *i.e.* the bispectrum components.[5] The code LAMMPS[6] has been used to generate the bi-spectrum components. In this framework, the ML model reads

$$T^m = \sum_i^{N_\mathrm{a}} T^m(i) = \sum_i^{N_\mathrm{a}} \sum_j^{N_j} \alpha_j^m(i) B_j(i)\,, \tag{2}$$

where index i runs over the number of atoms N_a, the index j runs over the N_j bi-spectrum components, B_j, describing the atomic environment of the i-th atom, and α_j^m are the coefficients that need to be determined. For the training of this model we used linear Ridge regression:

$$\min_{\{\alpha_j\}} \left[\|T^m_{\mathrm{QM}}(\{r_i\}) - T^m_{\mathrm{ML}}(\{r_i\},\{\alpha_j^m\})\|^2 + \lambda \|\{\alpha_j^m\}\|^2 \right]\,. \tag{3}$$

where the first term corresponds to the canonical least-square-fitting of the T^m_{QM} first principles reference values, and the second one to the regularization term. Here λ was set to 10^{-2} for the training of $\mathbf{g_e}$ and 10^{-4} for the training of $\mathbf{A}$. The covariancy of the Ridge regression for tensorial properties was enforced as proposed recently.[4] In all cases the order $2J = 8$ for the bi-spectrum components, corresponding to 56 elements per atomic species, has been used. A correspondence between atomic species and chemical identity was enforced with exception of the Vanadyl's Oxygen, which has been treated as an additional atomic species. Therefore, a model with five atomic species and 280 free parameters was trained. The radial

cutoff R_{cut} used to build the bi-spectrum components have been optimised as to minimise the overall error and it was fixed to 3.5 Å. The definition of bi-spectrum components gives the possibility to differentiate atomic kinds with weights and atomic radii.[5] In this work we have set all the weights to unity and kept all the atomic radii equal to 0.5. The latter condition corresponds to using the same R_{cut} for every species. Training curves of $\mathbf{g_e}$, both at the CASSCF and DFT level of theory, and $\mathbf{A}$ are provided as Supplementary Materials. The error associated with the ML model of $\mathbf{g_e}$ trained on CASSCF reference data is considerably higher than the one trained on DFT results. The former is therefore only used to estimate the error introduced in the estimation of relaxation time with spin-phonon coupling coefficients calculated with ML compared with a full ab-initio treatment. These results are provided as Supplementary Materials.

Spin-Phonon Coupling Coefficients

The spin phonon coefficients relative to the $\mathbf{g_e}$ and $\mathbf{A}$ tensors have been calculated as numerical derivatives. Using the ML models, $\mathbf{A}$ and $\mathbf{g_e}$ were sampled along every pair of Cartesian molecular degrees of freedom in the range [-0.05Å: 0.05Å]×[-0.05Å: 0.05Å] for a total number of 100 points. All the 90 molecular degrees of freedom were considered. Considering two different magnetic properties, $\mathbf{A}$ and $\mathbf{g_e}$, a total of 819,000 ML evaluations were carried out. Each one of these 2-dimensional grids of points was interpolated with a two-variable third-order polynomial expression, $f(x,y) = c_{30}x^3 + c_{03}y^3 + c_{21}x^2y + c_{12}xy^2 + c_{20}x^2 + c_{02}y^2 + c_1xy + c_{10}x + c_{01}y + c_{00}$. The coefficients c_{01} and c_{10} correspond to first-order spin-phonon coupling coefficients, $\partial\mathbf{g_e}/\partial X_{is}$ or $\partial\mathbf{A}/\partial X_{is}$, while the coefficient c_{11}, c_{20} and c_{02} corresponds to mixed and diagonal second-order derivatives such as $\partial^2\mathbf{g_e}/\partial X_{is}\partial X_{jt}$ or $\partial^2\mathbf{A}/\partial X_{is}\partial X_{jt}$. Translational invariance conditions were enforced on the calculated derivatives of the spin Hamiltonian tensors as discussed in Supplementary Materials. All the results presented in the main manuscript have been obtained with spin-phonon coupling coefficients calculated starting from machine learning models trained on DFT reference values for both $\mathbf{A}$ and $\mathbf{g_e}$.

Spin-phonon coupling coefficients calculated with machine learning models trained on $\mathbf{g_e}$ values obtained by CASSCF were only used for comparison with previous results on Direct relaxation.[1] A discussion of the latter is provided here as Supplementary Materials.

Spin-Phonon Coupling Translational Invariance

Translational invariance conditions were enforced on the calculated derivatives of the spin Hamiltonian tensors by rescaling the values by a mean deviation of this condition. For instance, for the elements ab of the tensor $\mathbf{A}$, the correction for the s Cartesian direction reads

$$\Big(\frac{\partial A_{ab}}{\partial X_{is}}\Big) = \Big(\frac{\partial A_{ab}}{\partial X_{is}}\Big) - Dev_s\,, \quad Dev_s = \frac{1}{N}\sum_{i}^{N}\Big(\frac{\partial A_{ab}}{\partial X_{is}}\Big)\,, \tag{4}$$

where N is the number of atoms in the molecule. An equivalent expression is used for the diagonal components of the second-order derivatives. We note that this correction is small for the spin-phonon coupling coefficients obtained with ML and including all the atoms in the model, but it might become significant when the estimations of spin-phonon coupling coefficients is carried out considering only a fraction of the atoms and/or the numerical derivatives are computed on a small number of points. The Cartesian derivatives $(\partial \hat{H}_{\mathrm{s}}/\partial X_{is})$ and $(\partial^2 \hat{H}_{\mathrm{s}}/\partial X_{is}\partial X_{jt})$ have then been projected onto the normal modes. For the element ab of the tensor $\mathbf{A}$ it reads

$$\Big(\frac{\partial A_{ab}}{\partial Q_{\alpha\mathbf{q}}}\Big) = \sum_{l}^{N_{cells}}\sum_{is}^{N,3}\sqrt{\frac{\hbar}{N_q\omega_{\alpha\mathbf{q}}m_i}}e^{i\mathbf{q}\cdot\mathbf{R}_l}L_{is}^{\alpha\mathbf{q}}\Big(\frac{\partial A_{ab}}{\partial X_{is}^{l}}\Big)\,, \tag{5}$$

$$\Big(\frac{\partial^2 A_{ab}}{\partial Q_{\alpha\mathbf{q}}\partial Q_{\beta\mathbf{q}'}}\Big) = \sum_{l}^{N_{cells}}\sum_{v}^{N_{cells}}\sum_{is}^{N,3}\sum_{jt}^{N,3}\sqrt{\frac{\hbar}{N_q\omega_{\alpha\mathbf{q}}m_i}}\sqrt{\frac{\hbar}{N_q\omega_{\beta\mathbf{q}'}m_j}}e^{i\mathbf{q}\cdot\mathbf{R}_l}e^{i\mathbf{q}'\cdot\mathbf{R}_v}L_{is}^{\alpha\mathbf{q}}L_{jt}^{\beta\mathbf{q}'}\Big(\frac{\partial^2 A_{ab}}{\partial X_{is}^{l}\partial X_{jt}^{v}}\Big)\,, \tag{6}$$

where X_{is}^{l} is the s Cartesian coordinate of the i-th atom of N with mass m_i, inside the unit-cell replica at position $\mathbf{R}_l$, and N_q is the total number of q-points used.

Spin Relaxation Calculations

For all the simulations, an initial density matrix corresponding to a pure state with maximum spin polarization was used. The full non-secular Redfield equations were solved and used to propagate the total spin density matrix. All the results have been obtained by converging the phonon lifetime to the harmonic limit. The Dirac's Delta functions present in $G^{1-\mathrm{ph}}$ and $G^{2-\mathrm{ph}}$ have been evaluated as a Gaussian function in the limit for infinite q-points and vanishing Gaussian breadth. For one-phonon processes, a grid of 64^3 q-points and a Gaussian breadth of 1 cm^{-1} was estimated to accurately reproduce this limit for all the temperature and field values investigated. For two-phonon relaxation, a grid of 2^3 q-points and a Gaussian of 1 cm^{-1} was enough to converge the results. Convergence tests for the one-phonon processes were presented before,[1] while those for two-phonon relaxation are available as Supporting Materials. The phenomenological modulation of phonon lifetime only affects the direct relaxation, by slowing it down as discussed previously,[1] while only a slight effect is observed on Raman relaxation. The magnetization dynamics of the electronic spin was monitored in time by calculating $\vec{\mathbf{M}} = \mathrm{Tr}\{\hat{\rho}^s(t)\vec{\mathbf{S}}\}$, where $\vec{\mathbf{S}}$ is the electronic spin operator. The relaxation time τ was obtained by fitting $M_z(t)$ with an exponential equation, $M_z(t) = M_z(0)exp(-t/\tau) + M(\infty)$.

Derivation of the Non-Secular Redfield Equations for Two-Phonon Processes.

Let us define a general spin Hamiltonian $\hat{H}_{\rm s}$, the phonons Hamiltonian $\hat{H}_{\rm ph}$ and the spin-phonon coupling Hamiltonian $\hat{H}_{\rm sph}$ as

$$\hat{H}_{\rm s} = \sum_{v} \hat{H}^{v} \,, \quad \hat{H}_{\rm ph} = \sum_{\alpha\mathbf{q}} \hbar\omega_{\alpha\mathbf{q}}(\hat{n}_{\alpha\mathbf{q}} + \frac{1}{2}) \,, \quad \hat{H}_{\rm sph} = \frac{1}{2}\sum_{\alpha\mathbf{q}}\sum_{\beta\mathbf{q}'}\sum_{v}\Big(\frac{\partial^2 \hat{H}^{v}}{\partial Q_{\alpha\mathbf{q}}\partial Q_{\beta\mathbf{q}'}}\Big)\hat{Q}_{\alpha\mathbf{q}}\hat{Q}_{\beta\mathbf{q}'} \,, \tag{7}$$

where the index v runs over all the terms of the spin Hamiltonian and $\hat{H}_{\rm sph}$ include the modulation of the spin Hamiltonian by two phonons at the time. The dynamics of the spin and bath systems can be described by means of density operator ρ, whose equation of motion in the interaction picture reads:

$$\frac{d\hat{\rho}(t)}{dt} = -\frac{i}{\hbar}[\hat{H}_{\rm sph}(t), \hat{\rho}(t)] \tag{8}$$

As the interest is on dynamics of only spin degrees of freedom it is convenient to define a reduced density operator taking trace over bath degrees of freedom: $\hat{\rho}^{\rm s}(t) = tr_B(\hat{\rho}(t))$. After a formal integration of equation (8):

$$\frac{d\hat{\rho}^{\rm s}(t)}{dt} = -\frac{1}{\hbar^2}\int_0^t ds \quad tr_B[\hat{H}_{\rm sph}(t), [\hat{H}_{\rm sph}(s), \hat{\rho}(s)]] \,. \tag{9}$$

The first step in the derivation of the Redfield equations is the *Born* approximation, that assumes the absence of quantum correlation between spins and phonons in virtue of their weak coupling, and reads $\hat{\rho}(t) = \hat{\rho}^{\rm s}(t) \otimes \hat{\rho}^{B}_{\rm eq}$, where $\hat{\rho}^{B}_{\rm eq}$ is the equilibrium phonons bath density matrix.

Next, the *Markov* approximation is carried out assuming the vibrational degrees of freedom to relax much faster than the spin system. To do so, the substitution $t' = t - s$ should be

done and the t' superior integration boundary should be brough to $+\infty$:

$$\frac{d\hat{\rho}^{\mathrm{s}}(t)}{dt} = -\frac{1}{\hbar^2}\int_0^{\infty} dt' tr_B[\hat{H}_{\mathrm{sph}}(t), [\hat{H}_{\mathrm{sph}}(t-t'), \hat{\rho}^{\mathrm{s}}(t)\otimes\hat{\rho}^B_{\mathrm{eq}}]] \,. \tag{10}$$

It is convenient to introduce a simplified notation where $\hat{V}^{v\alpha\mathbf{q}\beta\mathbf{q}'} = \left(\partial^2\hat{H}^v/\partial Q_{\alpha\mathbf{q}}\partial Q_{\beta\mathbf{q}'}\right)$ and substitute the definition of $\hat{H}_{\mathrm{sph}}$, as from Eq. 7, into Eq. 10 to obtain

$$\frac{d\hat{\rho}^{\mathrm{s}}(t)}{dt} = -\frac{1}{4\hbar^2}\int_0^{\infty} dt' \sum_v 2\sum_{\alpha\mathbf{q}}\sum_{\beta\mathbf{q}'}\Big\{ \tag{11}$$

$$\left[\hat{V}^{v\alpha\mathbf{q}\beta\mathbf{q}'}(t)\hat{V}^{v\alpha-\mathbf{q}\beta-\mathbf{q}'}(t-t')\hat{\rho}^s(t) - \hat{V}^{v\alpha\mathbf{q}\beta\mathbf{q}'}(t)\hat{\rho}^s(t)\hat{V}^{v\alpha-\mathbf{q}\beta-\mathbf{q}'}(t-t')\right] \tag{12}$$

$$Tr_B\left(\hat{Q}_{\alpha\mathbf{q}}(t)\hat{Q}_{\beta\mathbf{q}'}(t)\hat{Q}_{\alpha-\mathbf{q}}(t-t')\hat{Q}_{\beta-\mathbf{q}'}(t-t')\hat{\rho}^B_{\mathrm{eq}}\right) - \tag{13}$$

$$\left[\hat{V}^{v\alpha\mathbf{q}\beta\mathbf{q}'}(t-t')\hat{\rho}^s(t)\hat{V}^{v\alpha-\mathbf{q}\beta-\mathbf{q}'}(t) - \hat{\rho}^s(t)\hat{V}^{v\alpha\mathbf{q}\beta\mathbf{q}'}(t-t')\hat{V}^{v\alpha-\mathbf{q}\beta-\mathbf{q}'}(t)\right] \tag{14}$$

$$Tr_B\left(\hat{Q}_{\alpha\mathbf{q}}(t-t')\hat{Q}_{\beta\mathbf{q}'}(t-t')\hat{Q}_{\alpha-\mathbf{q}}(t)\hat{Q}_{\beta-\mathbf{q}'}(t)\hat{\rho}^B_{\mathrm{eq}}\right)\Big\} \tag{15}$$

where the terms $\int_0^{\infty} dt' e^{-i\omega_{ij}t'} Tr_B\left(\hat{Q}_{\alpha\mathbf{q}}(t)\hat{Q}_{\beta\mathbf{q}'}(t)\hat{Q}_{\alpha\mathbf{q}}(t-t')\hat{Q}_{\beta\mathbf{q}'}(t-t')\hat{\rho}^B_{\mathrm{eq}}\right)$ are the Fourier transforms of the two-phonon bath equilibrium correlation functions and depend on temperature. Eq. (15) was derived by taking into account that only products of terms such as $\hat{Q}_{\alpha\mathbf{q}}(t)\hat{Q}_{\alpha-\mathbf{q}}(t-t')$ would survive the thermal average and corresponds to transitions at non-zero energy. The factor 2 multiplying the summations on the indexes $\alpha\mathbf{q}\beta\mathbf{q}'$ accounts for the multiplicity of terms coming from developing the full product $\hat{Q}_{\alpha\mathbf{q}'}(t)\hat{Q}_{\beta\mathbf{q}''}(t)\hat{Q}_{\gamma\mathbf{q}''}(t-t')\hat{Q}_{\delta\mathbf{q}'''}(t-t')$.

By taking the matrix elements of $\hat{\rho}_{\mathrm{s}}(t)$ in the eigenket basis of $\hat{H}_{\mathrm{s}}|a\rangle = E_a|a\rangle$ it is possible to obtain:

$$\frac{d\rho^{\rm s}_{ab}(t)}{dt} = -\frac{1}{2\hbar^2}\int_0^\infty dt' \sum_v \sum_{\alpha\mathbf{q}} \sum_{\beta\mathbf{q}'} \sum_{cd} \Big\{ \tag{16}$$

$$\Big[V^{v\alpha\mathbf{q}\beta\mathbf{q}'}_{ac}(t) V^{v\alpha-\mathbf{q}\beta-\mathbf{q}'}_{cd}(t-t')\rho^{\rm s}_{db}(t) - V^{v\alpha\mathbf{q}\beta\mathbf{q}'}_{ac}(t)\rho^{\rm s}_{cd}(t) V^{v\alpha-\mathbf{q}\beta-\mathbf{q}'}_{db}(t-t')\Big] \tag{17}$$

$$Tr_B\Big(\hat{Q}_{\alpha\mathbf{q}}(t)\hat{Q}_{\beta\mathbf{q}'}(t)\hat{Q}_{\alpha-\mathbf{q}}(t-t')\hat{Q}_{\beta-\mathbf{q}'}(t-t')\hat{\rho}^B_{\rm eq}\Big) - \tag{18}$$

$$\Big[V^{v\alpha\mathbf{q}\beta\mathbf{q}'}_{ac}(t-t')\rho^{\rm s}_{cd}(t) V^{v\alpha-\mathbf{q}\beta-\mathbf{q}'}_{db}(t) - \rho^{\rm s}_{ac}(t) V^{v\alpha\mathbf{q}\beta\mathbf{q}'}_{cd}(t-t') V^{v\alpha-\mathbf{q}\beta-\mathbf{q}'}_{db}(t)\Big] \tag{19}$$

$$Tr_B\Big(\hat{Q}_{\alpha\mathbf{q}}(t-t')\hat{Q}_{\beta\mathbf{q}'}(t-t')\hat{Q}_{\alpha-\mathbf{q}}(t)\hat{Q}_{\beta-\mathbf{q}'}(t)\hat{\rho}^B_{\rm eq}\Big)\Big\} \tag{20}$$

Making the time dependencies of spin degrees of freedom explicit by going back to the Scroedinger picture, $V_{ab}(t) = \langle a|e^{iH_0 t}Ve^{-iH_0 t}|b\rangle = e^{i\omega_{ab}t}V_{ab}$, and doing some algebra it is possible to arrive at the two-phonon contribution of the non-secular Redfield equations

$$\frac{d\rho^{\rm s}_{ab}(t)}{dt} = \sum_{cd} e^{i(\omega_{ac}+\omega_{db})t} R^{2-{\rm ph}}_{ab,cd}\rho^{\rm s}_{cd}(t)\,, \tag{21}$$

where

$$R^{2-\mathrm{ph}}_{ab,cd} = -\frac{1}{2\hbar^2}\sum_{v}\sum_{\alpha\mathbf{q}}\sum_{\beta\mathbf{q}'} \tag{22}$$

$$\Big\{\sum_{j}\delta_{bd}V^{v\alpha\mathbf{q}\beta\mathbf{q}'}_{aj}V^{v\alpha-\mathbf{q}\beta-\mathbf{q}'}_{jc}\int_0^\infty dt' e^{-i\omega_{jc}t'}Tr_B\Big(\hat{Q}_{\alpha\mathbf{q}}(t)\hat{Q}_{\beta\mathbf{q}'}(t)\hat{Q}_{\alpha-\mathbf{q}}(t-t')\hat{Q}_{\beta-\mathbf{q}'}(t-t')\hat{\rho}^B_{\mathrm{eq}}\Big)$$

(23)

$$-V^{v\alpha\mathbf{q}\beta\mathbf{q}'}_{ac}V^{v\alpha-\mathbf{q}\beta-\mathbf{q}'}_{db}\int_0^\infty dt' e^{-i\omega_{db}t'}Tr_B\Big(\hat{Q}_{\alpha\mathbf{q}}(t)\hat{Q}_{\beta\mathbf{q}'}(t)\hat{Q}_{\alpha-\mathbf{q}}(t-t')\hat{Q}_{\beta-\mathbf{q}'}(t-t')\hat{\rho}^B_{\mathrm{eq}}\Big)$$

(24)

$$-V^{v\alpha\mathbf{q}\beta\mathbf{q}'}_{ac}V^{v\alpha-\mathbf{q}\beta-\mathbf{q}'}_{db}\int_0^\infty dt' e^{-i\omega_{ac}t'}Tr_B\Big(\hat{Q}_{\alpha\mathbf{q}}(t-t')\hat{Q}_{\beta\mathbf{q}'}(t-t')\hat{Q}_{\alpha-\mathbf{q}}(t)\hat{Q}_{\beta-\mathbf{q}'}(t)\hat{\rho}^B_{\mathrm{eq}}\Big)$$

(25)

$$+\sum_{j}\delta_{ca}V^{v\alpha\mathbf{q}\beta\mathbf{q}'}_{dj}V^{v\alpha-\mathbf{q}\beta-\mathbf{q}'}_{jb}\int_0^\infty dt' e^{-i\omega_{dj}t'}Tr_B\Big(\hat{Q}_{\alpha\mathbf{q}}(t-t')\hat{Q}_{\beta\mathbf{q}'}(t-t')\hat{Q}_{\alpha-\mathbf{q}}(t)\hat{Q}_{\beta-\mathbf{q}'}(t)\hat{\rho}^B_{\mathrm{eq}}\Big)\Big\}$$

(26)

Finally, we write explicitly the Fourier transform of the bath correlation functions, starting from substituting the relation between the normal modes of vibration $\hat{Q}_{\alpha\mathbf{q}}$ and the creation (annihilation) operators $\hat{a}^\dagger$ ($\hat{a}$) and their time evolution

$$\hat{Q}_{\alpha\mathbf{q}} = \frac{1}{\sqrt{2}}(\hat{a}^\dagger_{\alpha\mathbf{q}}+\hat{a}_{\alpha-\mathbf{q}}), \quad e^{i\hat{H}_{ph}t}\hat{a}^\dagger_{\alpha\mathbf{q}}e^{-i\hat{H}_{ph}t} = e^{i\omega_{\alpha\mathbf{q}}t}\hat{a}^\dagger_{\alpha\mathbf{q}}, \quad e^{i\hat{H}_{ph}t}\hat{a}_{\alpha\mathbf{q}}e^{-i\hat{H}_{ph}t} = e^{i\omega_{-\alpha\mathbf{q}}t}\hat{a}_{\alpha\mathbf{q}}. \tag{27}$$

This leads to

$$\int_0^\infty dt' e^{-i\omega_{ij}t'} Tr_B\Big(\hat{Q}_{\alpha\mathbf{q}}(t)\hat{Q}_{\beta\mathbf{q}'}(t)\hat{Q}_{\alpha-\mathbf{q}}(t-t')\hat{Q}_{\beta-\mathbf{q}'}(t-t')\hat{\rho}^B_{\rm eq}\Big) = \tag{28}$$

$$\frac{1}{4}\int_0^\infty dt' e^{-i\omega_{ij}t'} Tr_B\Big[e^{i\omega_{\alpha\mathbf{q}}t'}e^{i\omega_{\beta\mathbf{q}'}t'}\hat{a}^\dagger_{\alpha\mathbf{q}}\hat{a}_{\alpha\mathbf{q}}\hat{a}^\dagger_{\beta\mathbf{q}'}\hat{a}_{\beta\mathbf{q}'} + e^{-i\omega_{\alpha\mathbf{q}}t'}e^{-i\omega_{\beta\mathbf{q}'}t'}\hat{a}_{\alpha-\mathbf{q}}\hat{a}^\dagger_{\alpha-\mathbf{q}}\hat{a}_{\beta-\mathbf{q}'}\hat{a}^\dagger_{\beta-\mathbf{q}'} + \tag{29}$$

$$e^{i\omega_{\alpha\mathbf{q}}t'}e^{-i\omega_{\beta\mathbf{q}'}t'}\hat{a}^\dagger_{\alpha\mathbf{q}}\hat{a}_{\alpha\mathbf{q}}\hat{a}_{\beta-\mathbf{q}'}\hat{a}^\dagger_{\beta-\mathbf{q}'} + e^{-i\omega_{\alpha\mathbf{q}}t'}e^{i\omega_{\beta\mathbf{q}'}t'}\hat{a}_{\alpha-\mathbf{q}}\hat{a}^\dagger_{\alpha-\mathbf{q}}\hat{a}^\dagger_{\beta\mathbf{q}'}\hat{a}_{\beta\mathbf{q}'}\Big] = \tag{30}$$

$$\frac{1}{4}\int_0^\infty dt' e^{-i(\omega_{ij}-\omega_{\beta\mathbf{q}'}-\omega_{\alpha\mathbf{q}})t'}\hat{n}_{\alpha\mathbf{q}}\hat{n}_{\beta\mathbf{q}'} + \frac{1}{4}\int_0^\infty dt' e^{-i(\omega_{ij}+\omega_{\alpha\mathbf{q}}+\omega_{\beta\mathbf{q}'})t'}(\hat{n}_{\alpha\mathbf{q}}+1)(\hat{n}_{\beta\mathbf{q}'}+1) + \tag{31}$$

$$\frac{1}{4}\int_0^\infty dt' e^{-i(\omega_{ij}-\omega_{\alpha\mathbf{q}}t'+\omega_{\beta\mathbf{q}'})t'}\hat{n}_{\alpha\mathbf{q}}(\hat{n}_{\beta\mathbf{q}'}+1) + \frac{1}{4}\int_0^\infty dt' e^{-i(\omega_{ij}+\omega_{\alpha\mathbf{q}}-\omega_{\beta\mathbf{q}'})t'}(\hat{n}_{\alpha\mathbf{q}}+1)\hat{n}_{\beta\mathbf{q}'}\,, \tag{32}$$

where we have used the property $\omega_{\alpha\mathbf{q}} = \omega_{\alpha-\mathbf{q}}$ and the definition of the average phonon number $\bar{n}_{\alpha\mathbf{q}} = Tr_B\Big[\hat{a}^\dagger_{\alpha\mathbf{q}}\hat{a}_{\alpha\mathbf{q}}\Big]$.

Using the definition $\pi\delta(\omega) = \int_0^\infty dt' e^{-i\omega t'}$ we can rewrite the Raman Redfiled operator $R^{2-\rm ph}_{ab,cd}$ as

$$R^{2-\rm ph}_{ab,cd} = -\frac{\pi}{8\hbar^2}\sum_v\sum_{\alpha\mathbf{q}}\sum_{\beta\mathbf{q}'} \tag{33}$$

$$\Big\{\sum_j \delta_{bd}V^{v\alpha\mathbf{q}\beta\mathbf{q}'}_{aj}V^{v\alpha-\mathbf{q}\beta-\mathbf{q}'}_{jc}G^{2-\rm ph}(\omega_{jc},\omega_{\alpha\mathbf{q}},\omega_{\beta\mathbf{q}'}) - V^{v\alpha\mathbf{q}\beta\mathbf{q}'}_{ac}V^{v\alpha-\mathbf{q}\beta-\mathbf{q}'}_{db}G(\omega_{db},\omega_{\alpha\mathbf{q}},\omega_{\beta\mathbf{q}'}) \tag{34}$$

$$- V^{v\alpha\mathbf{q}\beta\mathbf{q}'}_{ac}V^{v\alpha-\mathbf{q}\beta-\mathbf{q}'}_{db}G^{2-\rm ph}(\omega_{ca},\omega_{\alpha\mathbf{q}},\omega_{\beta\mathbf{q}'}) + \sum_j \delta_{ca}V^{v\alpha\mathbf{q}\beta\mathbf{q}'}_{dj}V^{v\alpha-\mathbf{q}\beta-\mathbf{q}'}_{jb}G(\omega_{jd},\omega_{\alpha\mathbf{q}},\omega_{\beta\mathbf{q}'})\Big\}\,, \tag{35}$$

where

$$G^{2-\mathrm{ph}}(\omega_{ij},\omega_{\alpha\mathbf{q}},\omega_{\beta\mathbf{q}'}) =\delta(\omega_{ij}-\omega_{\alpha\mathbf{q}}-\omega_{\beta\mathbf{q}'})\bar{n}_{\alpha\mathbf{q}}\bar{n}_{\beta\mathbf{q}'}+\delta(\omega_{ij}+\omega_{\alpha\mathbf{q}}+\omega_{\beta\mathbf{q}'})(\bar{n}_{\alpha\mathbf{q}}+1)(\bar{n}_{\beta\mathbf{q}'}+1)+ \tag{36}$$

$$\delta(\omega_{ij}+\omega_{\alpha\mathbf{q}}-\omega_{\beta\mathbf{q}'})(\bar{n}_{\alpha\mathbf{q}}+1)\bar{n}_{\beta\mathbf{q}'}+\delta(\omega_{ij}-\omega_{\alpha\mathbf{q}}+\omega_{\beta\mathbf{q}'})\bar{n}_{\alpha\mathbf{q}}(\bar{n}_{\beta\mathbf{q}'}+1)\,. \tag{37}$$

Eqs. (7) and (27) assume the vibrational dynamics to be perfectly harmonic and undumped. In real systems, this approximation is never perfectly fulfilled and anharmonic terms need to be introduced in the definition of $\hat{H}_{\mathrm{ph}}$. In a perturbative regime this leads to an exponential decay profile of the phonons correlations functions with rate $\Delta/2\pi$. In this regime the Fourier transform of the two-phonon correlation function $G^{2-\mathrm{ph}}$ becomes

$$G^{2-\mathrm{ph}}(\omega_{ij},\omega_{\alpha\mathbf{q}},\omega_{\beta\mathbf{q}'}) = \frac{1}{\pi}\Big[\frac{\Delta_{\alpha\mathbf{q}\beta\mathbf{q}'}\bar{n}_{\alpha\mathbf{q}}\bar{n}_{\beta\mathbf{q}'}}{\Delta^2_{\alpha\mathbf{q}\beta\mathbf{q}'}+(\omega_{ij}-\omega_{\alpha\mathbf{q}}-\omega_{\beta\mathbf{q}'})^2}+\frac{\Delta_{\alpha\mathbf{q}\beta\mathbf{q}'}(\bar{n}_{\alpha\mathbf{q}}+1)(\bar{n}_{\beta\mathbf{q}'}+1)}{\Delta^2_{\alpha\mathbf{q}\beta\mathbf{q}'}+(\omega_{ij}+\omega_{\alpha\mathbf{q}}+\omega_{\beta\mathbf{q}'})^2}+ \tag{38}$$

$$\frac{\Delta_{\alpha\mathbf{q}\beta\mathbf{q}'}\bar{n}_{\alpha\mathbf{q}}(\bar{n}_{\beta\mathbf{q}'}+1)}{\Delta^2_{\alpha\mathbf{q}\beta\mathbf{q}'}+(\omega_{ij}-\omega_{\alpha\mathbf{q}}+\omega_{\beta\mathbf{q}'})^2}+\frac{\Delta_{\alpha\mathbf{q}\beta\mathbf{q}'}(\bar{n}_{\alpha\mathbf{q}}+1)\bar{n}_{\beta\mathbf{q}'}}{\Delta^2_{\alpha\mathbf{q}\beta\mathbf{q}'}+(\omega_{ij}+\omega_{\alpha\mathbf{q}}-\omega_{\beta\mathbf{q}'})^2}\Big]\,, \tag{39}$$

where $\Delta_{\alpha\mathbf{q}\beta\mathbf{q}'}=\Delta_{\alpha\mathbf{q}}+\Delta_{\beta\mathbf{q}'}$

Convergence of Machine Learning Results.

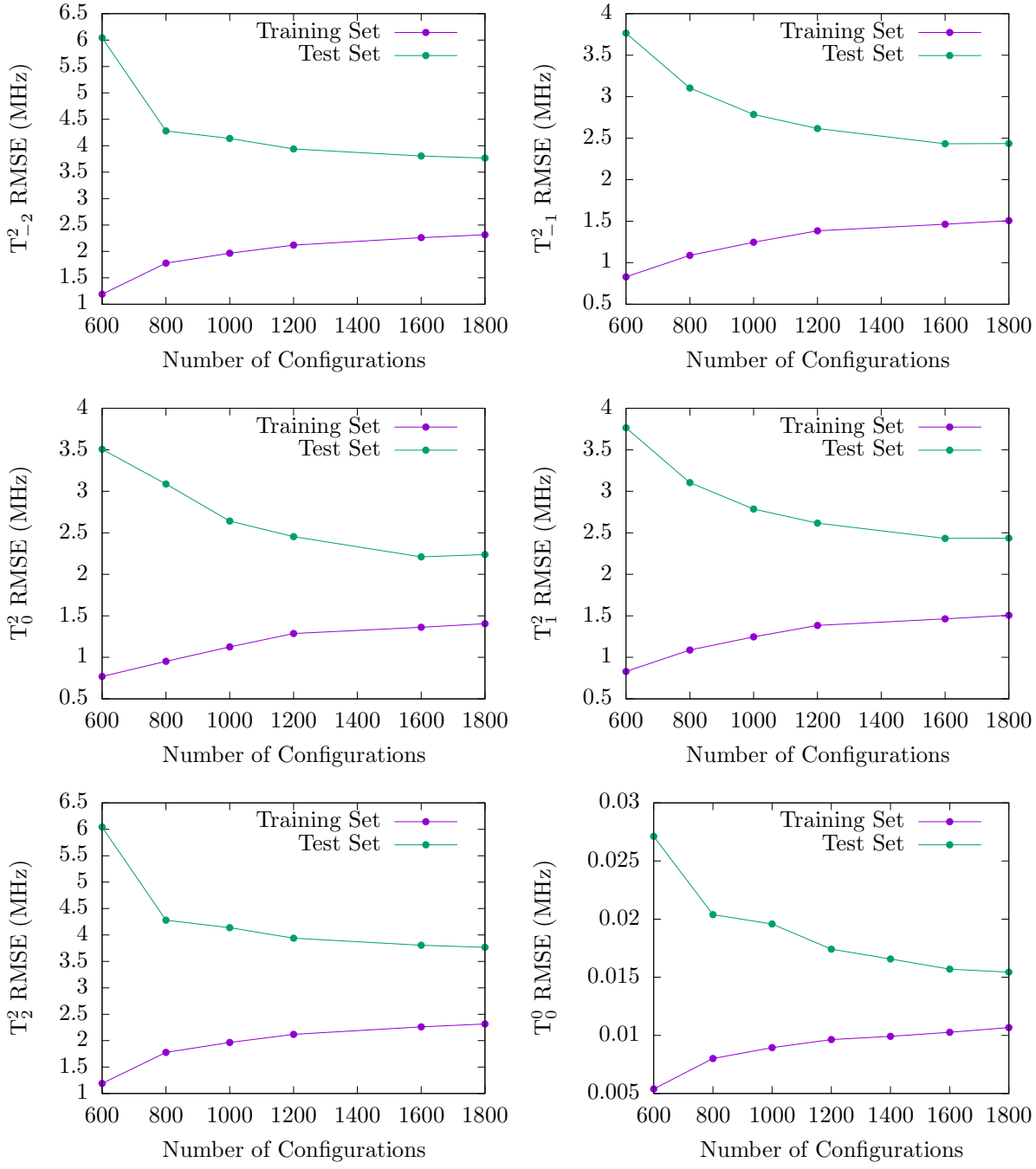

Supplementary Figure 1: **Training Curves for the A Tensor ML Regression.** The error on both training and test sets is reported as function of the training set size. The test set is always kept at its maximum size.

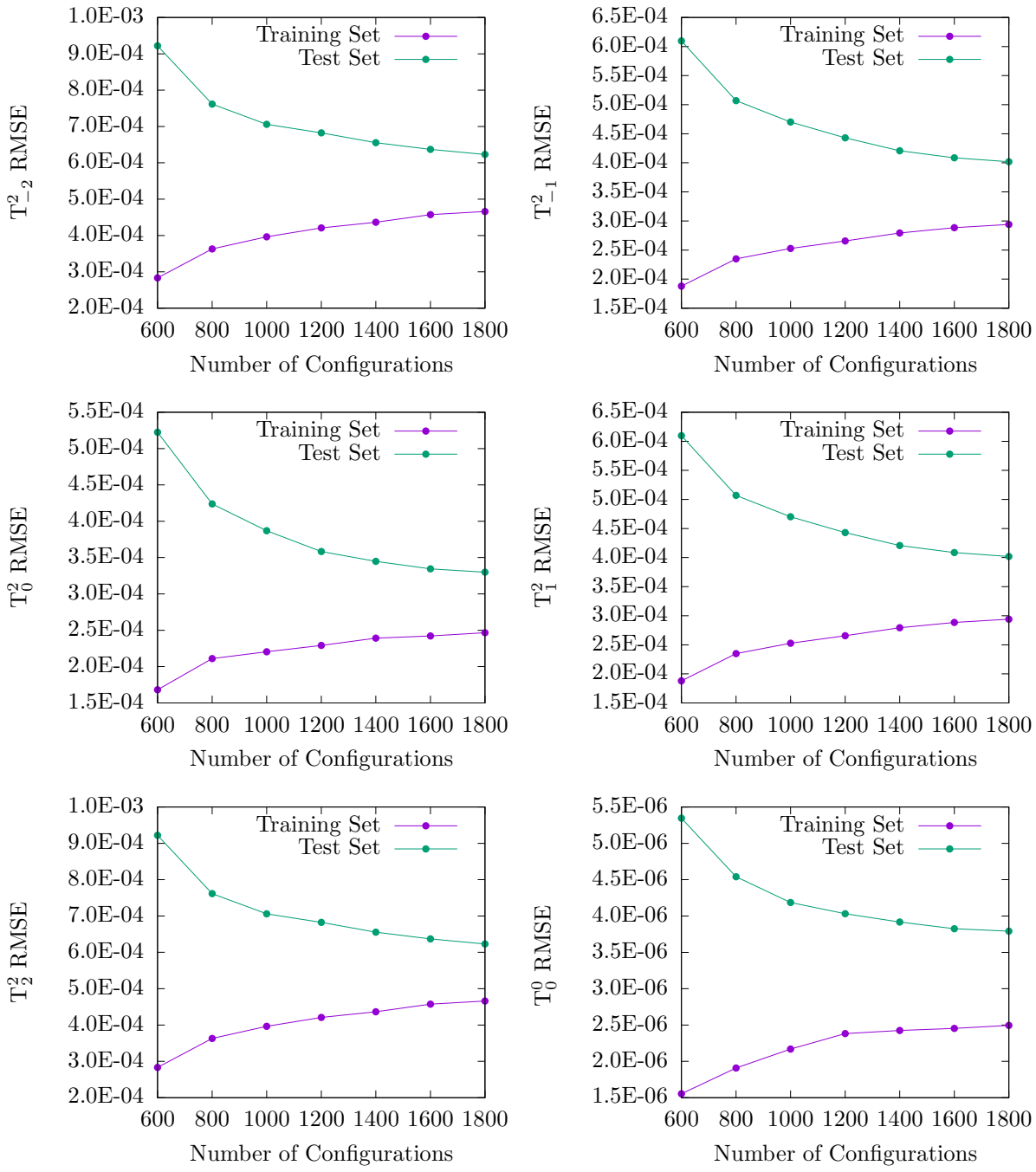

Supplementary Figure 2: **Training Curves of the g Tensor ML Regression.** The error on both training and test sets is reported as function of the training set size. The test set is always kept at its maximum size. Both training and test sets were calculated at the DFT level of theory.

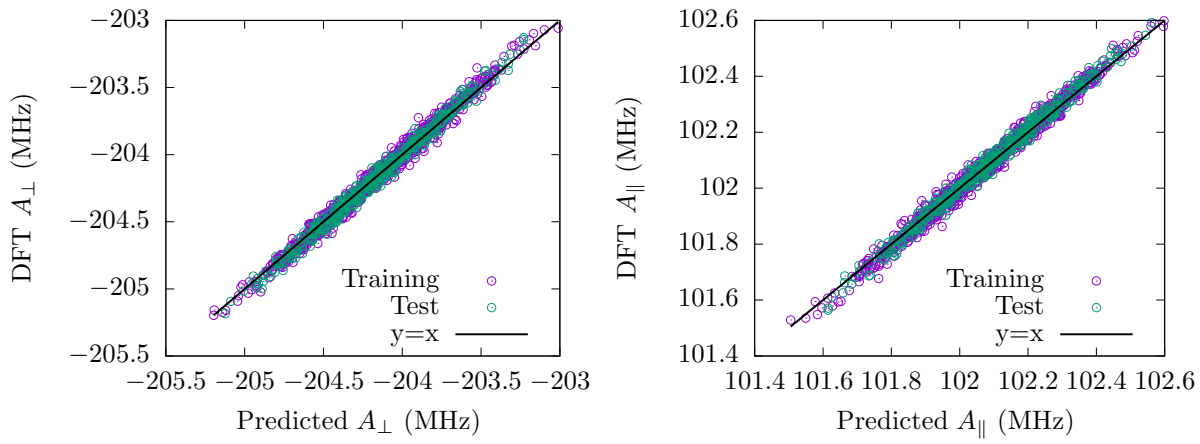

Supplementary Figure 3: **Comparison of DFT and ML prediction of Eigenvalues of the Traceless A Tensor.** The traceless tensor **A** is diagonalized and its eigenvalues are used to calculate $A_\perp$ and $A_\parallel$. The results for training and test sets are then compared among ML predictions and ab initio reference values.

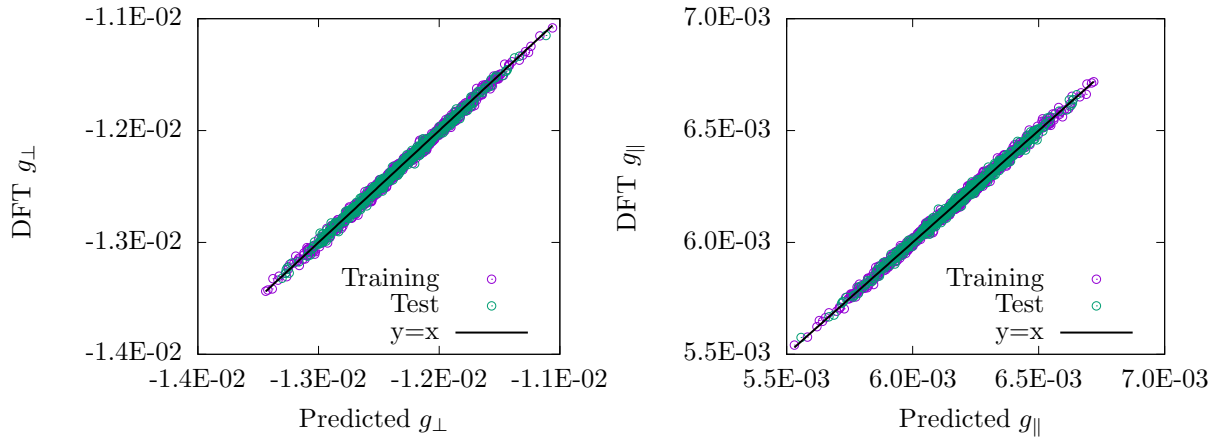

Supplementary Figure 4: **Comparison of DFT and ML prediction of Eigenvalues of the Traceless g Tensor.** The traceless tensor $\mathbf{g}_e$ is diagonalized and its eigenvalues are used to calculate $g_\perp$ and $g_\parallel$. The results for training and test sets are then compared among ML predictions and ab initio reference values.

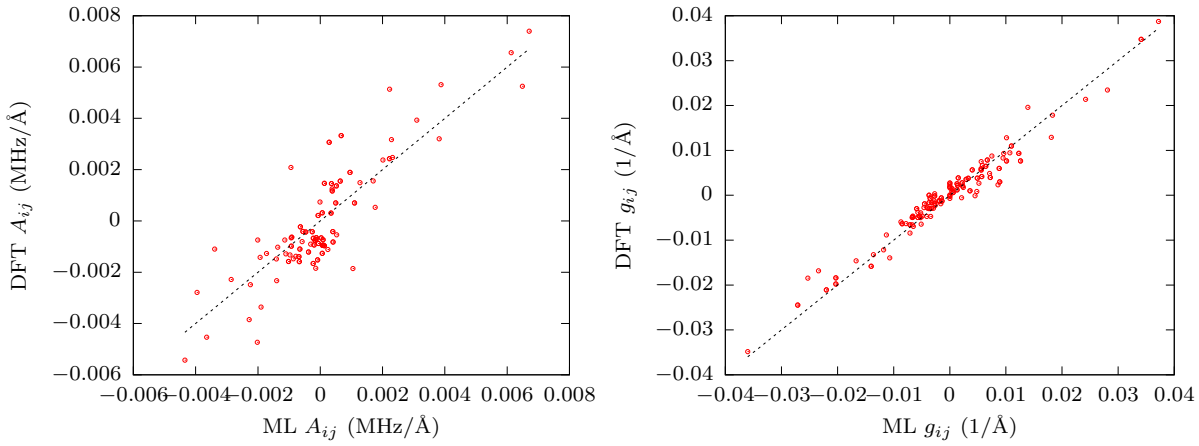

Supplementary Figure 5: **Comparison of DFT and ML prediction of first-order spin-phonon coupling.** The components of the tensors $\mathbf{g}_e$ and $\mathbf{A}$ have been numerically differentiated at the first order with respect to the Cartesian positions of the atoms of the first coordination shell. The left and right panels report the comparison between these quantities calculated with ML and DFT, for $\mathbf{A}$ and $\mathbf{g}_e$, respectively. A Pearson correlation coefficient of 0.85 and 0.98 was calculated for for $\mathbf{A}$ and $\mathbf{g}_e$, respectively.

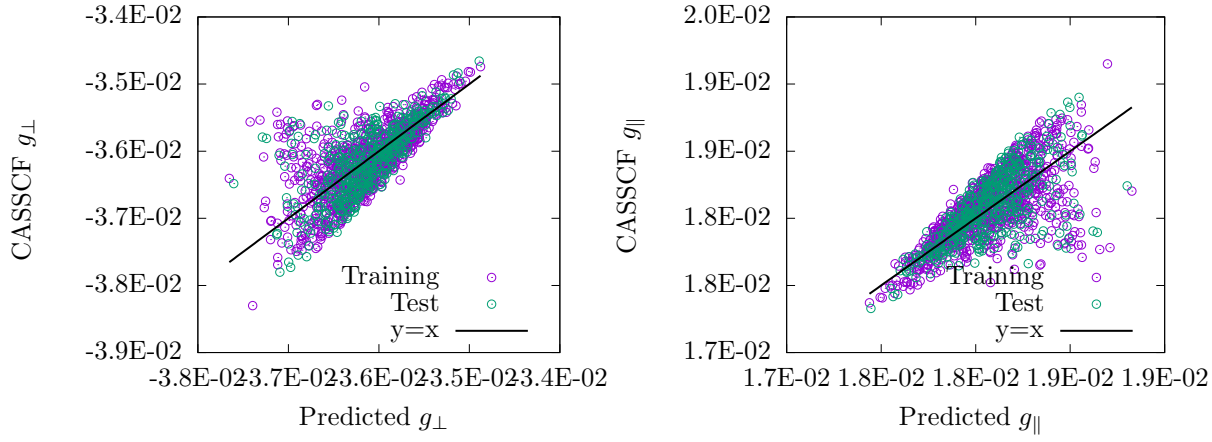

Supplementary Figure 6: **Comparison of CASSCF and ML prediction of Eigenvalues of the Traceless g Tensor.** The traceless tensor $\mathbf{g}_e$ is diagonalized and its eigenvalues are used to calculate $g_\perp$ and $g_\parallel$. The results for training and test sets are then compared among ML predictions and ab initio reference values.

Convergence of Relaxation Time.

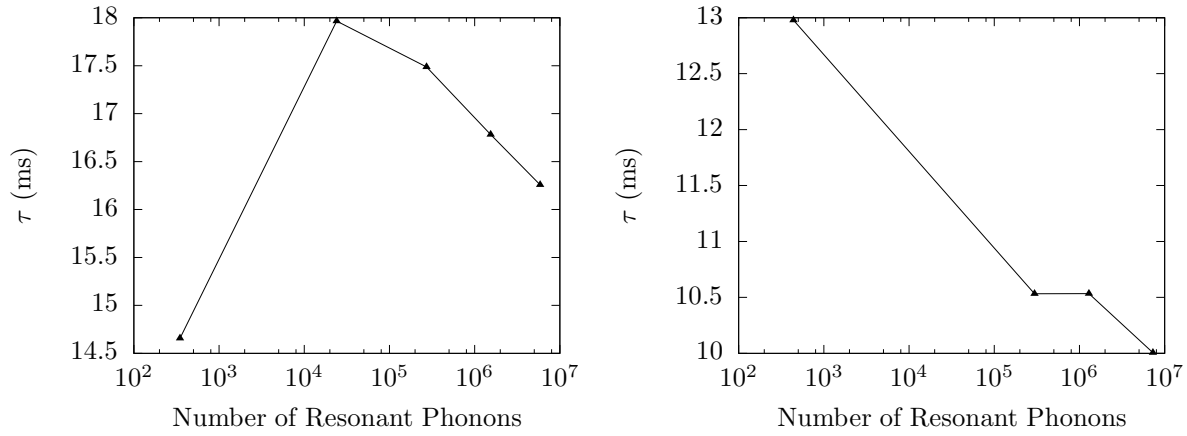

Supplementary Figure 7: **Convergence of Raman Relaxation Time as Function of Brillouin Zone Integration Grid.** Relaxation time is calculated at $|B|$=0.1 T (left panel) and $|B|$=1.0 T (right panel) with uniform grids of points in Brillouin zone with mesh 2^3, 4^3, 6^3, 8^3 and 10^3. The temperature is set to 25 K for all the simulations. The x-axis reports the number of resonant phonons effectively included in the calculation of spin relaxation. The Dirac's delta function used to estimate the resonance condition was approximated with a Gaussian with smearing of 1 cm^{-1}.

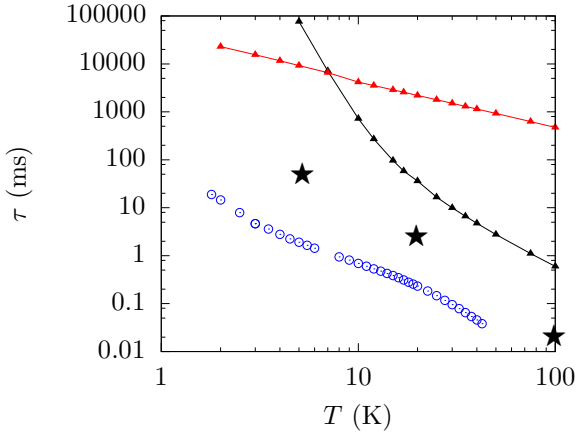

Supplementary Figure 8: **Spin-phonon relaxation time at 0.3T.** Computed direct (red line and squares), computed Raman (black line and triangles) and AC measured (blue line and circles) spin relaxation time as function of temperature T with an external magnetic field of 0.3 T. The star symbols correspond to the average T_1 obtained from X-Band EPR measurements of diluted samples, both solid-state and frozen solution.[7–10]

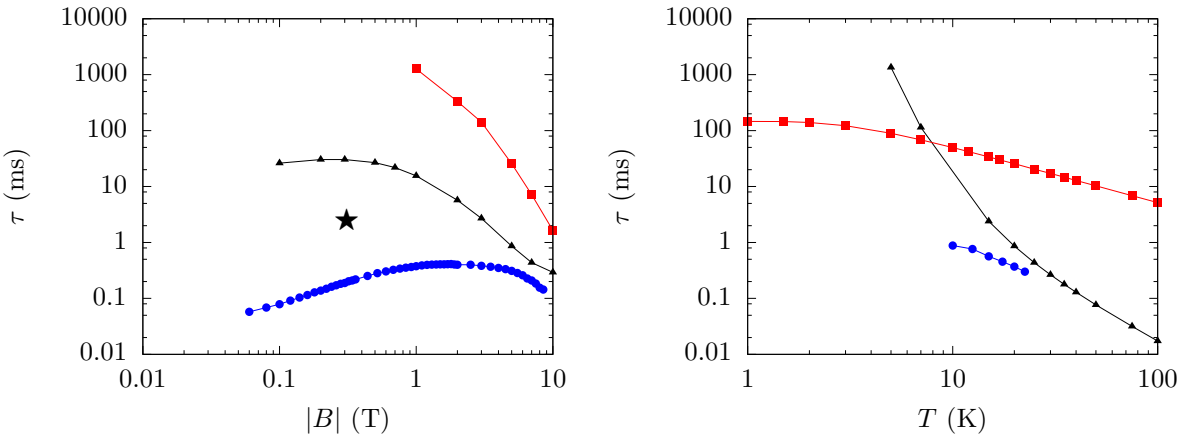

Supplementary Figure 9: **Spin relaxation with CASSCF.** The Raman and Direct spin relaxation time calculated using a machine-learning model for $\mathbf{g_e}$ trained on CASSCF. (Left Panel) Computed direct (red line and squares), computed Raman (black line and triangles) and AC measured (blue line and circles) spin relaxation time as function of the external magnetic field $|B|$ at 20 K. The star symbol corresponds to the average T_1 obtained from EPR measurements of magnetically diluted samples, both solid-state and frozen solution.[7–10] (Right Panel) Computed direct (red line and squares), computed Raman (black line and triangles) and AC measured (blue line and circles) spin relaxation time as function of temperature T with an external magnetic field of 5 T.

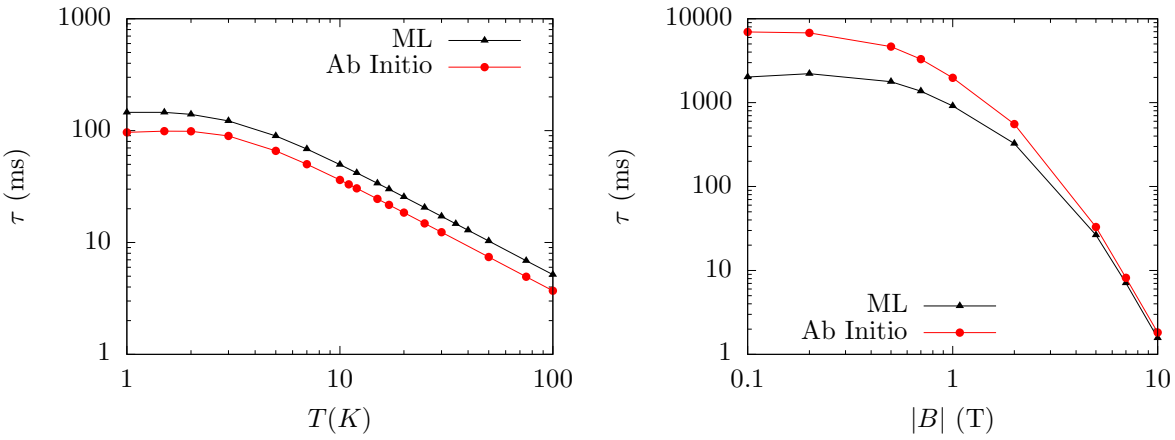

Supplementary Figure 10: **Validation of Spin Dynamics with Machine Learning.** The direct relaxation dynamics computed with spin-phonon coupling coefficients obtained by ML trained on CASSCF and by CASSCF directly.[1] The left panel reports the dynamics as function of temperature in external field of 5 T. The right panel reports the dynamics as function of the external field $|B|$ at 20 K. Considering the rather poor accuracy of the ML model trained on CASSCF the agreement is exceptionally good. Discrepancies only appear below 2 T, where phonons' numerical noise becomes important for Direct relaxation. Phonons involved in Raman relaxation have energies well above 10 cm^{-1} and these results suggest a good accuracy of ML in quantify them.

Supplementary References

(1) A. Lunghi, S. Sanvito, *Sci. Adv.* **5**, eaax7163 (2019).

(2) F. Neese, *Wiley Interdiscip. Rev. Comput. Mol. Sci.* **2**, 73 (2012).

(3) J. P. Perdew, K. Burke, Y. Wang, *Phys. Rev. B* **54**, 533 (1996).

(4) A. Lunghi, S. Sanvito, *J. Phys. Chem. C* **124**, 5802 (2020).

(5) A. P. Thompson, L. P. Swiler, C. R. Trott, S. M. Foiles, G. J. Tucker, *J. Comput. Phys.* **285**, 316 (2015).

(6) S. Plimpton, *J. Comput. Phys.* **117**, 1 (1995).

(7) M. Atzori, *et al.*, *J. Am. Chem. Soc.* **138**, 2154 (2016).

(8) C. J. Yu, *et al.*, *J. Am. Chem. Soc.* **138**, 14678 (2016).

(9) M. Atzori, *et al.*, *J. Am. Chem. Soc.* **138**, 11234 (2016).

(10) M. Atzori, *et al.*, *Inorg. Chem.* **57**, 731 (2018).